

LARGE EDDY SIMULATIONS OF ASYMMETRIC TURBULENT HYDROGEN JETS ISSUING FROM REALISTIC PIPE GEOMETRIES

Maxwell, B.M.¹, Soleimani nia, M.¹, Oshkai, P.¹, and Djilali, N.¹

¹Institute for Integrated Energy Systems, University of Victoria,
PO Box 1700 STN CSC, Victoria BC, V8W 2Y2, Canada, brianmaxwell@uvic.ca

ABSTRACT

In the current study, a Large Eddy Simulation strategy is applied to model the dispersion of compressible turbulent hydrogen jets issuing from realistic pipe geometries. The work is novel, as it explores the effect of jet densities and Reynolds numbers on vertical buoyant jets, as they emerge from the outer wall of a pipe, through a round orifice, perpendicular to the mean flow within the pipe. An efficient Godunov solver is used, and coupled with Adaptive Mesh Refinement to provide high resolution solutions only in areas of interest. The numerical results are validated against physical experiments of air and helium, which allows a degree of confidence in analysing the data obtained for hydrogen releases. The results show that the jets investigated are always asymmetric. Thus, significant discrepancies exist when applying conventional round jet assumptions to determine statistical properties associated with gas leaks from pipelines.

1.0 INTRODUCTION

In recent years, with the emergence of new hydrogen technologies, there has been much focus on advancing research to understand ignition behaviour of hydrogen leaks in order to assess explosion and safety hazards. A number of experiments have shown, to date, that hydrogen jets are easily ignitable, and have a wide range of ignition limits (between 4% to 75% by volume) [1]. It is therefore of paramount interest to understand the dispersive nature of hydrogen, a highly compressible gas, in order to adequately develop codes and standards. The current study attempts to determine, through numerical simulation, the dispersion of compressible hydrogen leaks, from a realistic piping configuration, in order to determine the extent of ignition limits associated with the respective release conditions considered. The piping arrangement considered here is novel, as we examine gas dispersion from vertical jets emerging through circular holes located in the side wall of a round pipe, perpendicular to the mean flow within the pipe.

Traditionally, scientific research has been limited to compressible fuel leaks through flat surfaces, aligned in the direction of the mean flow origin. To date, much is known about the axisymmetric and self-similar nature of such jet configurations, emerging through round holes, for a wide range of Reynolds numbers and gas densities. Statistical analysis has been performed, and theory developed, for many physical experiments [2–5]. Advances in computational resources have also allowed numerical simulation, through Large Eddy Simulation (LES), to prove useful for determining entire flow fields of such round jets [1]. In general, data has been collected for air, helium, and CO₂ jets, due to the reactive nature of hydrogen. However, numerical simulation has also proved useful in determining ignition limits, for hydrogen in particular, in such configurations [1]. In addition to round jets, several investigations [6, 7] have also been carried out for jet releases through different shaped orifices of varying aspect ratios, also through flat plates, in order to determine how asymmetric behaviours emerge, such as the *axis-switching* phenomenon. In other investigations, buoyancy effects on horizontal jets have also been investigated [8]. All of this work has been of prime importance to determine dispersive nature of gases, for fuel-safety purposes, for gas leaks of various hole geometries and flow conditions. In reality, however, accidental fuel leaks would not be limited to flows through flat surfaces. From a practical point of view, flow patterns and dispersion of gas originating from holes in the side walls of circular pipes should also be investigated. To date, to the authors knowledge, no such investigation has been formally published.

In the current investigation, jets issuing from such realistic geometry are considered. Turbulent vertical jets flowing through a 2mm diameter round hole in the side of a 6.36mm diameter round pipe are modelled numerically, through LES. The investigation, thus considers flow through a curved surface from a source whose original velocity component is nearly perpendicular to the direction of the jet itself. The fluids considered are air, helium, and hydrogen. Different fluid densities, ratio of specific heats, and buoyancy are considered accordingly. The flow Mach numbers and Reynolds numbers of the jets range from 0.4 to 1.5 and 18,000 to 56,000, respectively. These compressible and turbulent flow conditions are consistent with physical experiments of air and helium releases [9], which have been conducted as part of this work for numerical validation purpose. An efficient Godunov solver is used, and coupled with Adaptive Mesh Refinement (AMR) to provide high-resolution solutions only in areas of interest. This work aims to highlight the asymmetric nature of the jet issuing from such a geometry. The results obtained suggest that significant discrepancies exist, when applying conventional assumptions for round jets issuing through flat surfaces, to determine statistical properties associated with gas leaks from pipelines.

2.0 METHODOLOGY

2.1 Governing Equations

For flows which are turbulent and compressible, the gas dynamic evolution is governed by the compressible Navier-Stokes equations. In order to account for the full spectrum of length scales, resulting from large flow velocities with high Reynolds numbers (Re), the unresolved scales of the governing equations are filtered and modelled through the LES approach. Thus, the large-scale fluid motions are captured directly, while the small-scale contributions are modelled through source terms. The LES-filtered conservation equations for mass, momentum, and energy (sensible + kinetic) of a calorically perfect fluid system are given below in eqs. (1)-(3), respectively. Also, a transport equation (4) is included to describe the evolution of mass fraction (Y) associated with the jet gas. The governing equations are also supplemented by a one-equation Localized Kinetic energy Model [10], given by eq. (5). This describes the transport, production, and dissipation of the subgrid kinetic energy (k^{sgs}) associated with subgrid velocity fluctuations. Finally, the equations of state are given by (6). The equations presented here are given in non-dimensional form, where the various properties are normalized by the reference quiescent state. Favre-average filtering is achieved by letting $\tilde{f} = \overline{\rho f} / \bar{\rho}$, where f represents one of the many state variables. ρ , p , e , T , and \mathbf{u} refer to the density, pressure, specific sensible + kinetic energy, temperature, and velocity vector, respectively. Other usual properties are the ratio of specific heats, γ , the kinematic viscosity, ν , the resolved shear stress tensor, $\bar{\boldsymbol{\tau}}$, the Prandtl number, Pr , and the Schmidt number, Sc . Also, subgrid contributions due to buoyancy have been accounted for, where \mathbf{g} is the gravitational acceleration.

$$\frac{\partial \bar{\rho}}{\partial t} + \nabla \cdot (\bar{\rho} \tilde{\mathbf{u}}) = 0 \quad (1)$$

$$\frac{\partial (\bar{\rho} \tilde{\mathbf{u}})}{\partial t} + \nabla \cdot (\bar{\rho} \tilde{\mathbf{u}} \tilde{\mathbf{u}}) + \nabla \bar{p} - \nabla \cdot \bar{\rho} (\nu + \nu_t) \left(\nabla \tilde{\mathbf{u}} + (\nabla \tilde{\mathbf{u}})^T - \frac{2}{3} (\nabla \cdot \tilde{\mathbf{u}}) \mathbf{I} \right) = \bar{\rho} \mathbf{g} \quad (2)$$

$$\frac{\partial (\bar{\rho} \tilde{e})}{\partial t} + \nabla \cdot \left((\bar{\rho} \tilde{e} + \bar{p}) \tilde{\mathbf{u}} - \tilde{\mathbf{u}} \cdot \bar{\boldsymbol{\tau}} \right) - \nabla \cdot \left(\bar{\rho} \left(\frac{\gamma}{\gamma - 1} \right) \left(\frac{\nu}{Pr} + \frac{\nu_t}{Pr_t} \right) \nabla \tilde{T} \right) = \bar{\rho} \tilde{\mathbf{u}} \cdot \mathbf{g} \quad (3)$$

$$\frac{\partial (\bar{\rho} \tilde{Y})}{\partial t} + \nabla \cdot (\bar{\rho} \tilde{\mathbf{u}} \tilde{Y}) - \nabla \cdot \left(\bar{\rho} \left(\frac{\nu}{Sc} + \frac{\nu_t}{Sc_t} \right) \nabla \tilde{Y} \right) = 0 \quad (4)$$

$$\frac{\partial (\bar{\rho} k^{sgs})}{\partial t} + \nabla \cdot (\bar{\rho} \tilde{\mathbf{u}} k^{sgs}) - \nabla \cdot \left(\frac{\bar{\rho} \nu_t}{Pr_t} \nabla k^{sgs} \right) = -\frac{\nu_t}{Pr_t} \nabla \bar{\rho} \cdot \mathbf{g} + \dot{P} - \bar{\rho} \epsilon \quad (5)$$

$$\tilde{e} = \frac{\bar{p} / \bar{\rho}}{(\gamma - 1)} + \frac{1}{2} \tilde{\mathbf{u}} \cdot \tilde{\mathbf{u}} + k^{sgs} \quad \text{and} \quad \frac{\bar{p}}{\bar{\rho}} = R \tilde{T} \quad (6)$$

The various state variables have been normalized such that

$$\rho = \frac{\hat{\rho}}{\hat{\rho}_o}, \quad \mathbf{u} = \frac{\hat{\mathbf{u}}}{\hat{c}_o}, \quad p = \frac{\hat{p}}{\hat{\rho}_o \hat{c}_o^2} = \frac{\hat{p}}{\gamma \hat{p}_o}, \quad T = \frac{\hat{T}}{\gamma \hat{T}_o}, \quad x = \frac{\hat{x}}{\hat{D}}, \quad t = \frac{\hat{t}}{\hat{D}/\hat{c}_o}, \quad R = \frac{\hat{R}}{\hat{R}_o} = \frac{1/\hat{W}}{1/\hat{W}_o}, \quad (7)$$

where the subscript ‘o’ refers to the reference state, the hat superscript refers to a dimensional quantity, \mathbf{I} is the identity matrix, c is the speed of sound, W is the molecular weight, and D is a reference length scale. This reference length scale is taken as the diameter of the orifice through which the gas exits the pipe. Here, the subgrid kinetic energy, k^{sgs} , is produced at the same rate from which large-scale turbulent motions are dissipated, on the LES-scale, through the turbulent kinematic viscosity, ν_t . The rate of production and dissipation of k^{sgs} are given by

$$\dot{P} = \bar{\rho} \nu_t \left(\nabla \tilde{\mathbf{u}} + (\nabla \tilde{\mathbf{u}})^T - \frac{2}{3} (\nabla \cdot \tilde{\mathbf{u}}) \mathbf{I} \right) \cdot (\nabla \tilde{\mathbf{u}}) \quad \text{and} \quad \epsilon = \pi \left(\frac{2k^{sgs}}{3C_\kappa} \right)^{3/2} / \bar{\Delta}. \quad (8)$$

Finally, a Smagorinsky-type model is applied to describe ν_t in terms of k^{sgs} through

$$\nu_t = \frac{1}{\pi} \left(\frac{2}{3C_\kappa} \right)^{3/2} \sqrt{k^{sgs}} \bar{\Delta}. \quad (9)$$

Here, C_κ is the *Kolmogorov constant*, whose value is set to a typical value of $C_\kappa = 1.5$. For simplicity, the LES filter size, $\bar{\Delta}$, is assumed to be equal to the (local) minimum grid spacing. It is noted, however, that this assumption may introduce some errors at fine-coarse cell interfaces when coupled with AMR [11]. Finally, for the helium case, owing to differences in γ , eq. (4) is replaced with

$$\frac{(\partial \tilde{\rho} \tilde{G})}{\partial t} + \nabla \cdot (\tilde{\rho} \tilde{\mathbf{u}} \tilde{G}) - \nabla \cdot \left(\tilde{\rho} \left(\frac{\nu}{Sc} + \frac{\nu_t}{Sc_t} \right) \nabla \tilde{G} \right) = 0 \quad (10)$$

where

$$\tilde{Y} = \frac{\tilde{G} - G_{\text{air}}}{G_{\text{He}} - G_{\text{air}}} \quad \text{and} \quad G = \left(\frac{1}{\gamma - 1} \right). \quad (11)$$

Although this method, in conservative form, is known to introduce pressure oscillations, which originate from material interfaces [12], it is necessary to ensure the correct mathematical representation of the diffusion process. While non-conservative approaches have been proven to eliminate such pressure oscillation errors [12], they can also converge to incorrect solutions with respect to diffusion [13]. Thus, the conservative scheme has been adopted for helium, noting that hydrogen simulations do not suffer this deficiency since γ shares the same value as air. Furthermore, nearly isothermal jets are considered, where minimal heat diffusion effects are expected. For practical purpose, γ is evaluated from \tilde{G} directly, as no suitable alternative exists in the LES framework.

2.2 Numerical Implementation

In order to solve the system of equations (1) through (5), an efficient second order accurate *exact* Godunov compressible flow solver [14], which features a symmetric monotized central flux limiter [15], is applied to treat the convection terms consisting of potentially different γ values on each side of the interface. The diffusive terms are handled explicitly in time using the forward Euler method, and spatially discretized using second order accurate central differences. Structured Cartesian grids are applied in order to take advantage of AMR [16] for increased efficiency. The grid is refined, on a per cell-basis, in regions close to the physical pipe, and also where the jet gas mass ($\tilde{\rho} \tilde{Y}$) changes by more than 0.01% locally between existing grid levels. Also, once a cell is refined, it remains refined for the duration of the simulation. This avoids complications which arise due to cell-derefinement and re-refinement [17]. Finally, the jet is refined to a minimum grid size of $D/16$ up to $10D$ downstream from the orifice in order to capture fine scale turbulent motions in the near field. Beyond $10D$ downstream, the jet is only refined to a minimum grid size of $D/8$. These resolutions were both found to yield converged solutions of the mass flux ejecting through the orifice. A detailed grid convergence study is currently being conducted.

2.3 Domain and Model Parameters

The numerical domain containing the pipe and jet configuration is shown in Fig. 1. The pipe has an outer diameter of $3.18D$ (6.36mm) with a wall thickness of $0.41D$ (0.82mm). The hole, through which gas escapes, has a diameter of $\hat{D} = 2\text{mm}$. The domain itself spans $32D$ in each direction. The inlet boundary condition (BC) is imposed on one side of the pipe, which uses a Digital Filtering Generation method [18] to generate the appropriate second order turbulence characteristics according to well-documented experimental measurements of turbulence in pipe flow [19]. A wall BC is imposed on the other side of the pipe, which causes the flow to stagnate within the pipe up the the hole through which gas escapes. The top BC of the domain is a pressure outlet type. The remaining 5 BCs are symmetry type slip walls, and are sufficiently far away from the jet to prevent interference. The initial condition, within the domain, is entirely air at ambient conditions ($\hat{T}_o = 300\text{K}$ and $\hat{p}_o = 101.3\text{kPa}$).

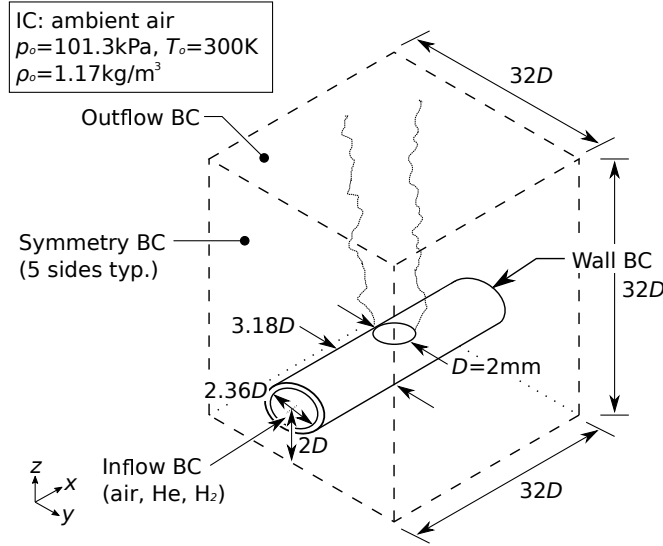


Figure 1: Computational domain with initial and boundary conditions (not to scale).

In all three simulations, the average momentum flux $(\overline{\rho u})_{\text{flux}}$ has been matched. To achieve this, the inlet pressure has been varied, through trial and error, to obtain the desired $(\overline{\rho u})_{\text{flux}}$ and average flow velocity (u_j) , which correspond to the experiments [9]. Here, the instantaneous $(\rho u)_{\text{flux}}$ was measured directly on an x - y plane corresponding to the hole location on the outer edge of the pipe, at $z = 0$, where

$$(\rho u)_{\text{flux}} = \int_{z=0} \rho u_z u_z dA. \quad (12)$$

The momentum flux is then time-averaged across 1000 samples. The resulting $(\overline{\rho u})_{\text{flux}}$, jet velocity (u_j) , and other relevant fluid properties are given in Table 1. The transport properties have been evaluated at equimolar conditions, and are assumed constant for simplicity. For the turbulent transport properties of all three jets, $Sc_t = 0.7$ and $Pr_t = 0.8$ and are also assumed constant.

Table 1: Model Parameters.

Jet	$\hat{\rho}_j$ (kg/m ³)	\hat{u}_j (m/s)	Re	$(\hat{\rho}\hat{u})_{\text{flux}}(N)$	γ	$\hat{\nu}$ (m ² /s)	Pr	Sc
air	1.17	141.7	17,824	0.0335	1.4	1.59×10^{-5}	0.714	0.707
He	0.164	368.1	38,545	0.0317	1.67	1.91×10^{-5}	0.607	0.626
H ₂	0.082	528.4	55,915	0.0328	1.4	1.89×10^{-5}	0.556	0.609

3.0 RESULTS

3.1 Time-Averaged Flow Fields

Time-averaged flow fields, showing the velocity magnitudes for the air and helium simulations, are shown in Fig. 2. Also shown, for comparison, are the corresponding flow fields obtained experimentally using Particle Image Velocimetry. All simulations presented have been averaged over 1000 samples in time, once the quasi-steady jet evolution has been established. For air and helium, this sampling period corresponds to 267 and 583 eddy-turnover times, respectively. The eddy-turnover time is defined here as $\tau = D/u_j$. In all cases, the jet is always established with a slight deflection from the vertical z -axis, in the initial direction of flow within the pipe. This can be observed on the x - z planes which pass through the geometric centre of the orifice ($y = 0$), as seen in the figure. In this plane, some notable differences are observed between the experiments and simulations with respect to spreading of the jet. In the experiments, significant jet spreading is observed as soon as the jet emerges from the orifice. In the simulations, however, there is a slightly longer potential core region, and the jet does not appear to begin spreading until several diameters downstream from the orifice. Also, in the experiments, the extents at which the jet spreads appears to be much more smooth and linear compared to the simulations. Some asymmetry is observed, in both the experiments and simulations, with respect to jet spreading near the core, close to the orifice. In the air simulations and experiments, it appears that the jet experiences more spreading on the left of the core, initially. While the helium experiment also shows this trend, the helium simulation is found to spread more on the right of the core, initially. Downstream, however, the experimental jets appear to be more symmetric compared to the simulations. All simulations appear to develop a higher velocity bias on the left side of the jet, thus suggesting there is more spreading overall on the right side of the jet in the far field. In the simulations, there are also some differences in the jet spreading flow patterns, between air and helium, around $z = 4 - 10D$. In the helium case, there appears to be a sudden expansion of the jet around $z = 4D$, followed by slight contraction around $z = 8D$. For air, although more subtle, these flow features occur at $z = 8D$ and $z = 15 - 18D$, respectively. For the experiments, the flow patterns are qualitatively similar for both air and helium, and do not exhibit the contraction in spreading observed numerically.

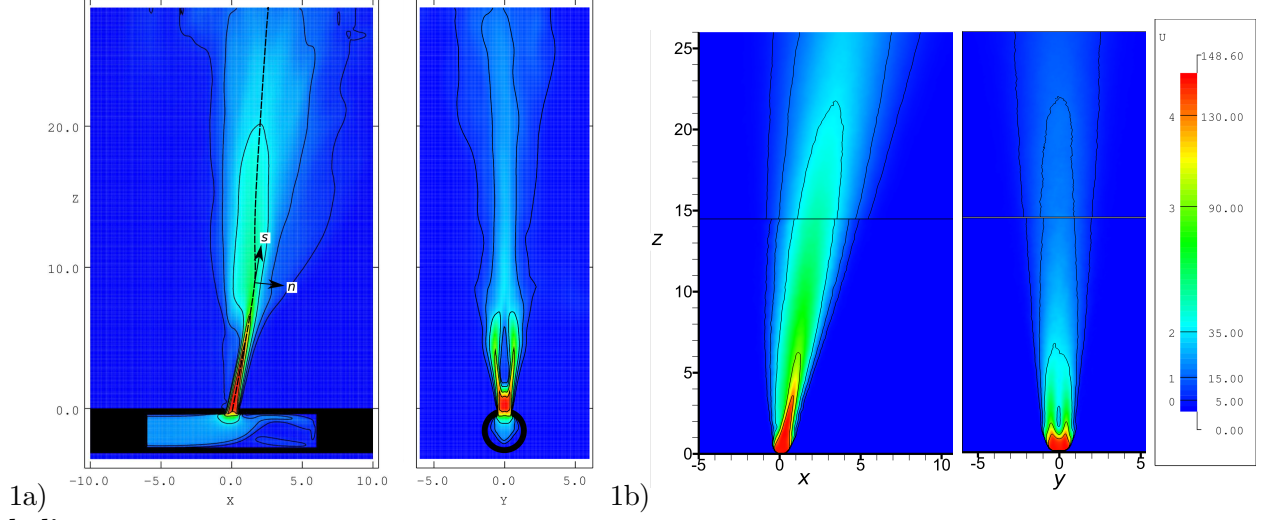
On the y - z planes, which pass through the geometric centre of the orifice ($x = 0$), the jet deflection causes what appears to be a shortening of the potential core (on this plane) in all cases. Also, near the orifice, two high-velocity regions are observed on each side of the z axis, about $y = 0$, at roughly $y \pm 0.5 - 1D$. There is also a very low velocity region at $y = 0$, in between these two high velocity regions. This is much more pronounced in the simulations compared to experiments, which is probably due to less initial jet spreading from the potential core regions. Thus, for the simulations, there is a very distinct *dead-zone* around $z \sim 5D$, which was not present in the experiments. Finally, in the simulations, there appears to be a contraction of the jet-spread around $z \sim 10D$. This is probably attributed to the movement of the jet away from the y - z plane located at $x = 0$. Although not shown here, the hydrogen flow field, which was averaged over $\Delta\tau = 660$, was found to be qualitatively similar to the helium case.

3.2 The Jet Centreline

In order to measure the trajectory of each jet, whose deflection from the vertical (z) axis was observed in Fig. 2, the (x, y) locations of the maximum velocity magnitude ($|\mathbf{u}|_{\max}$) were determined at discrete heights (along the z -axis) in increments of $1D$ from the orifice. These jet trajectories, from experiments and the simulations, are shown in Fig. 3 for all cases. Also shown are the computed centre of mass locations (C.M.) for each simulation. The C.M., as a function of height (z), was determined by extracting x - y slices at each discrete height along the z -axis, also in increments of $1D$, and evaluating the centroid associated with the average mass flux of the jet through each slice. For a given z location,

$$x_{\text{C.M.}} = \frac{\int (\overline{\rho u_z Y}) x \, dx \, dy}{\int (\overline{\rho u_z Y}) \, dx \, dy} \quad \text{and} \quad y_{\text{C.M.}} = \frac{\int (\overline{\rho u_z Y}) y \, dx \, dy}{\int (\overline{\rho u_z Y}) \, dx \, dy}. \quad (13)$$

air:



helium:

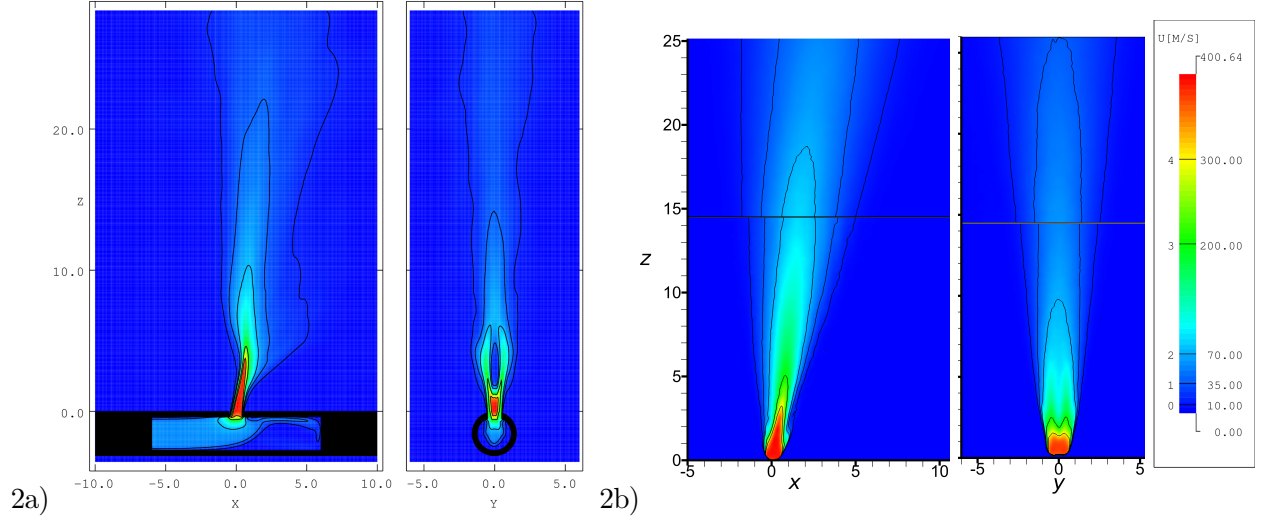


Figure 2: Average velocity in $x-z$ and $y-z$ planes for 1) air and 2) helium, obtained from a) LES and b) experiments. Note: Hydrogen (not shown) was found to be qualitatively similar to the helium simulation.

In Fig. 3, it is clear that the simulation jet centres, determined from $|\mathbf{u}|_{\max}$, do not match those obtained from the experiments for helium and air beyond $z > 4$ and $z > 10$, respectively. These locations correspond to the extents of the potential cores observed from the simulations in Fig. 2. On the other hand, the C.M. locations match very well the jet centre-lines obtained from experiments through the entire range of heights away from the orifice. Clearly the simulations appear to exhibit a slight departure of the $|\mathbf{u}|_{\max}$ location from the actual jet centroid. Also, the $|\mathbf{u}|_{\max}$ locations contain significant scatter beyond the jet cores, especially for the air simulation. Lines of best-fit, using linear regression to power-law expressions, were obtained for the scattered data regions of each gas, as shown in the figure. From the air simulation and experiment, the C.M. curve and experimental jet centre follows a very linear trajectory from the orifice, located at $z = 0$. This is to be expected, as there are no buoyancy effects present. For the helium and hydrogen jets, however, a slight ‘kink’ is noticed in the trajectory around $z \sim 5$, near the extent of the potential-core region. From this point, the jet trajectory curves upwards, leading to a departure from the air curve.

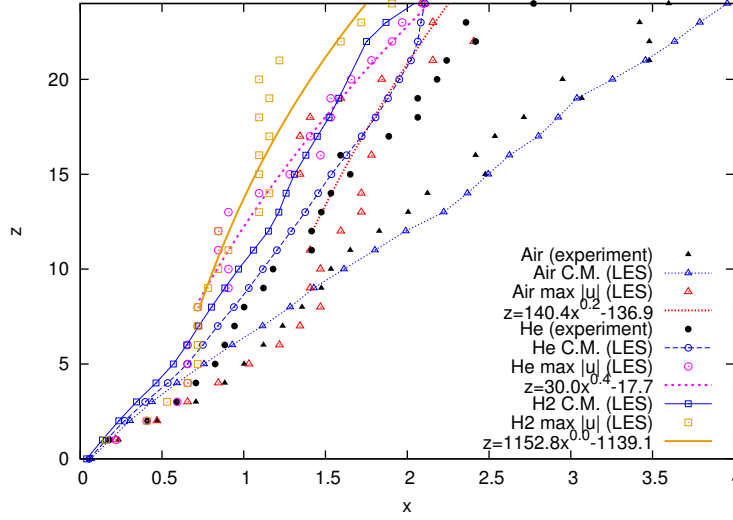


Figure 3: Jet centre-lines taken along the location of maximum velocity ($|\mathbf{u}|_{\max}$) locations from experiments and simulations, and also the centre of mass (C.M.) locations obtained from the simulations.

3.3 Properties Along the Jet Centreline

In Fig. 4a, the velocity decay along the jet centre-lines, determined from $|\mathbf{u}|_{\max}$, are presented for all cases, both numerically and experimentally. Also shown, for comparison, are velocity decay correlations [20], which have been determined from dozens of compressible subsonic and supersonic axisymmetric round jet experiments, for the range jet conditions that encompass the current investigation. For the air jet, the simulation is found to match closely the velocity decay obtained from experiment. For the helium jet, however, the simulation has a much faster decay rate compared to experiment. Despite this, both exhibit the same trend, where helium is found to decay faster than air. It is also observed that the experiments have a shorter potential-core region. In general, the experimental velocity decays begin around $1D$ before the simulations. Upon comparison to the Witze correlations, the trends obtained from the experiments and simulations are found to be in agreement with those decay rates expected for axisymmetric round jets. Hydrogen was found to decay the quickest, while air was found to decay the slowest. However, in all cases, the decay rates observed in the current investigation decay much faster compared to the axisymmetric round jet correlations.

In Fig. 4b, the jet widths ($2L_{1/2}$) have been obtained by determining the locations where $|\mathbf{u}| = 0.5|\mathbf{u}|_{\max}$ along lines which are orthogonal to the jet-centrelines. In the x - z plane, the orthogonal lines to the jet-centres, determined by $|\mathbf{u}|_{\max}$, have been indicated, previously, as coordinate n in Fig. 2, and data is available from both the simulations and the experiments. In y - z planes, the orthogonal lines to the jet-centres are collinear with the y direction owing to symmetry of the jet. Furthermore, jet widths along y are only available from simulation. In the x - z plane (along n), the air and helium jet spreading, from experiments and simulations, is found to be comparable for both gases. In the near field, significant jet spreading does not occur until about $z \sim 5$ for experiment and $z \sim 7 - 8$ for the simulations, which coincide with the potential-core extents of the jet. In fact, only in the far field does helium have a slightly faster spreading rate compared to air, experimentally, while the simulations have the opposite trend. Despite this, both the experiments and simulations are in agreement in order of magnitude. In the y - z plane (along y), the jet spreading obtained from the simulations deviate from those obtained in the x - z plane around $z = 12$. In fact, the jet widths in the y direction are found to remain fairly constant through the far-field. Also shown in Fig. 4b are jet spreading rates obtained from axisymmetric round jets for various Re [3, 4]. It was found that the jet spreading of air and helium in the y direction,

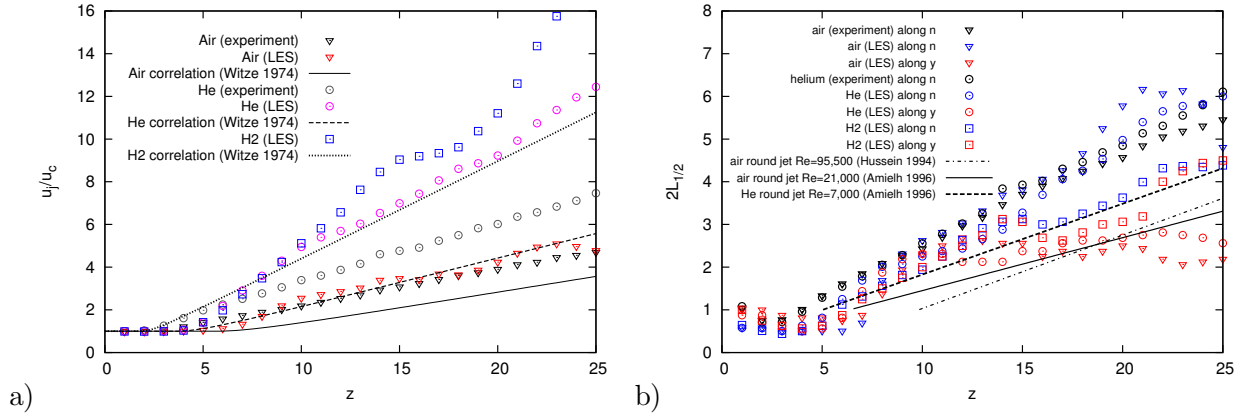
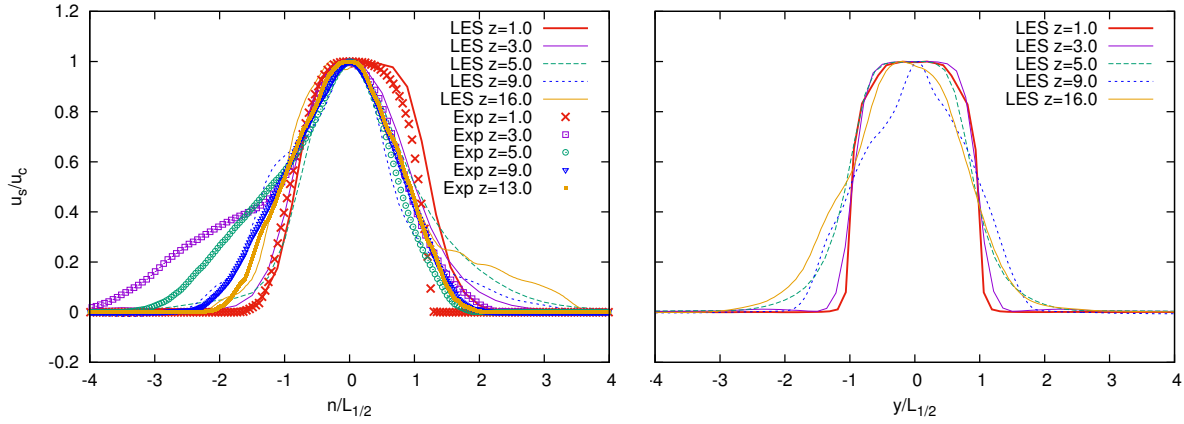


Figure 4: a) Jet velocity decay and b) jet widths ($2L_{1/2}$) obtained along the $|u|_{\max}$ centre-lines, from simulations and experiments. Note, the direction n refers to lines which are normal to the centre-line, coplanar with the x - z axis (see the coordinate system in Fig. 2). Also, velocity decays and jet widths have been compared to axisymmetric round jet correlations [20] and experiments [3, 4], respectively.

air:



helium:

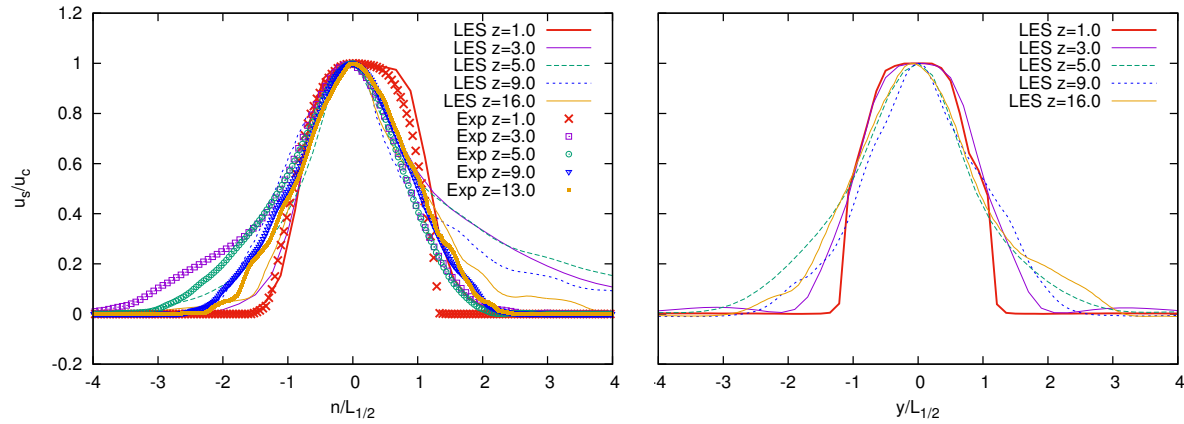


Figure 5: Average velocity profiles, along jet centre-lines, taken at various heights. Note, distances are normalized by the jet half widths ($L_{1/2}$) from Fig. 4b. Note: Hydrogen (not shown) was found to be qualitatively and quantitatively similar to both air and helium.

found numerically, compares well to the jet spreading of axisymmetric round jets, in terms of order of magnitude, while more jet spreading was found in the n direction. On the other hand, the hydrogen simulations are found to match well the round jet spreading rate in both directions.

Finally, average velocity profiles were obtained along the jet centre-line, determined by $|\mathbf{u}|_{\max}$, and presented in Fig. 5 for air and helium. In this figure, only the average velocity components along the jet centres (s direction), normalized by the local centre-line velocity, are presented. Numerically, these profiles are available along both the n and y directions, while experimental data is only available in the n direction. All distances are normalized by the local half width ($L_{1/2}$). In general, the simulated velocity profiles along the n direction compared well to the experiments for both air and helium. However, some differences are observed near the tail ends of the curves. The experiments are found to exhibit more velocity spreading to the left of the jet centre (in the $-n$ direction) in the near field ($z < 5$). On the other hand, the simulations are found to exhibit more velocity spreading to the right of the jet centre (in the $+n$ direction) in both the near and far fields. Despite this, the profiles near the jet centres, from $-1 < (n/L_{1/2}) < 1$, are found to agree well between experiment and simulation. In the y direction, the velocity profiles are found to be much more symmetric, as expected. Finally, The curves obtained for air, helium, and hydrogen (not shown) are found to be qualitatively similar to each other, noting the differences in velocity magnitude due to spreading beyond $z > \pm 1$ in the n direction.

4.0 DISCUSSION

4.1 Asymmetry of the Jet

The results, presented above, clearly reveal that for air and helium, asymmetric behaviour of the jet is observed. While hydrogen was found to develop axisymmetric spreading rates in the far field, it also displayed similar asymmetric behaviour in the near field. First, the perpendicular nature of the orifice, relative to the direction of flow within the pipe, causes a deflection of the jet away from the vertical axis. It is not yet clear how the deflection angles scale for each gas, however, heavier gases are found to deflect more than lighter gases, despite having equal momentum flux (force) ejecting through the orifice.

One notable ‘event’ is observed to occur for each gas, in the near field, between $z = 5 - 10$. Not only does this location correspond to the extent of the potential-core, in each case, but the simulations also observe the $|\mathbf{u}|_{\max}$ to deviate significantly from the C.M., previously shown in Fig. 3. The location of $|\mathbf{u}|_{\max}$ follows closely the C.M. up until $z \sim 8D$ for air and $z \sim 4D$ for helium and hydrogen. At this point, the location of $|\mathbf{u}|_{\max}$ remains constant in x until $z \sim 12D$ for air and $z \sim 8D$ for helium and hydrogen. Downstream, the location of $|\mathbf{u}|_{\max}$ travels to the right again. However, this location is then misaligned to the left of the C.M. (in the $-x$ direction), especially for the air simulation. It is noted, however, that the time interval at which data was collected is much better resolved for helium and hydrogen, in terms of $\Delta\tau$, compared to air. The data collected for air spans only $\Delta\tau = 267$, while helium and hydrogen are more than twice that value. This may also explain the large scatter of measurements, in $|\mathbf{u}|_{\max}$, collected for the air simulation, compared to the helium and hydrogen simulations.

In order to gain insight as to why the location of $|\mathbf{u}|_{\max}$ shifts from the right of the C.M. to the left, average velocity contours have been extracted on x - y planes at various heights, along z , for all three gases. Figure 6 shows these velocity contours for the helium simulation, although it is noted that the other gases are qualitatively similar in the near field. At the very start of the jet evolution, shown at $z = 0$, the initial jet is not circular. In fact, a velocity deficit exists near the left-most portion of the orifice, and also two regions on the right side, near $x = 0.25$ and $y \pm 0.3$. The velocity deficit on the left of the jet probably results from flow separation of the moving gas originating from inside the pipe, akin to flow over a backward step [21] or cavity [22]. The flow deficits on the right of the jet are probably caused by the curvature of the pipe diameter relative to the hole size. This remains to be investigated. Downstream, at $z = 3$, the flow pattern develops into a very asymmetric flow pattern. In fact, a void is

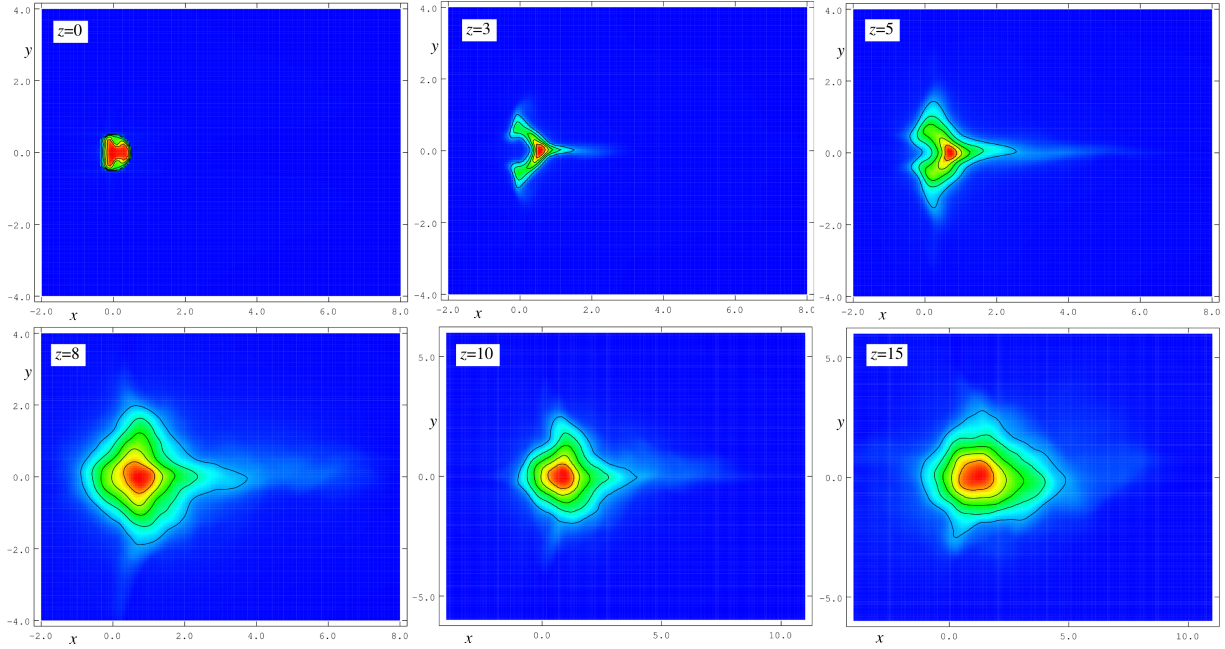


Figure 6: Average velocity contours in x - y planes for He. Note: H_2 and air are qualitatively similar.

created along the z axis centred at $x = y = 0$. Also, there exists significant flow on either side of the void in the $\pm y$ directions. As a result, the C.M. of the jet is found to be located to the left of the $|\mathbf{u}|_{\max}$ location. This flow pattern explains the two large velocity regions observed in the y - z planes of Fig. 2, both numerically and experimentally. Eventually, at $z = 5$, the void becomes consumed by the jet as mixing occurs. Eventually, by $z = 8$, the location of $|\mathbf{u}|_{\max}$ is located to the left of the C.M. Although significant mixing and jet spreading has occurred by this point, a portion of the jet remains asymmetric. In fact, the overall shape of the jet is stretched along the $+x$ direction, relative to the jet centre. From $x > 3$, there appears to be some minor secondary jetting along the $+x$ direction, which is not observed in any other direction. This secondary jetting is believed to contribute to the misalignment of the $|\mathbf{u}|_{\max}$ location with the C.M. By $z = 15$, the shape of the helium and air jets become elliptical. The jet remains somewhat asymmetric and experiences more jet spreading in the $+x$ direction compared to all other directions. This explains the large jet spreading along the n direction relative to the y direction, and also axisymmetric round jets [3, 4], as observed in Fig. 4b. The hydrogen simulation (not shown), on the other hand, was found to develop into a fairly round jet by $z = 15$. Although the $|\mathbf{u}|_{\max}$ was still misaligned with the C.M., the spreading rates in all directions were nearly equal, see Fig. 4b. Whether the air and helium jets considered here eventually becomes axisymmetric, in the far field, remains to be investigated. It is possible that the early symmetric development for hydrogen, compared to air and helium, may arise due to enhanced mixing associated with the supersonic nature of the jet.

4.2 Departures of Simulation From Experiment

In this investigation, several discrepancies were observed between the simulations and experiments. First, the appearance of ‘dead zones’ in the y - z planes of Fig. 2 were not so prevalent in the experiments. It was found that the experiments experienced much more mixing, from the onset of release, compared to the simulations. This had the effect of mitigating the numerically observed ‘dead zone’, and also shortened the potential-core length compared to the simulations. It is well known that turbulent mixing rates can reduce the potential-core length of a jet [23]. Thus, it is probably the case that persisting laminar conditions exist in the potential core due to insufficient integration time in the simulations. Despite this short coming in the near field, the simulations are found to capture the correct trends observed

experimentally and have provided some insight, physically, in terms of the asymmetric nature of the jet, which emerges radially from a pipe.

In terms of the velocity decay, the simulation captured well the experimental measurements for air. However, a significant deviation from experimental measurements was observed for the helium simulation. It is unclear why this departure between experiment and simulation exists. It is possible that errors associated with mixing in the two- γ model generates a faster velocity decay for helium compared to experiment. This is currently under investigation.

Finally, it has been observed that the location of $|\mathbf{u}|_{\max}$ is inconsistent between the simulations and experiments. From experiments, it was found that this location is relatively centred in the jet, along the n direction. In the simulations, however, the location of $|\mathbf{u}|_{\max}$ had a tendency to shift towards the left side of the jet C.M. location (in the $-x$ direction). Despite this, the numerical prediction of the C.M. was found to agree well with the $|\mathbf{u}|_{\max}$ location obtained from experiments. It is possible that longer sampling periods are required in order to accurately predict the position of $|\mathbf{u}|_{\max}$ numerically. This is especially true for the air simulation, for which $|\mathbf{u}|_{\max}$ was only evaluated for samples within $\Delta\tau = 267$, and contained a lot of scatter. Also, it is possible that the discrete nature of the wall boundaries of the pipe, due to the application of a Cartesian grid, may impact the flow evolution.

5.0 CONCLUSIONS

Here, a large-eddy-simulation strategy was developed to model compressible turbulent jets, of varying gas densities and Reynolds numbers, issuing from realistic pipe geometry. The fluids considered were air, helium, and hydrogen. The strategy was validated against a corresponding experimental investigation [9] accordingly. While it was found that the simulations did not capture the correct jet spreading and mixing in the near field, and thus the potential core length, the jet spreading, and average velocity profiles have been well recovered beyond the near-field. Furthermore, there is a significant discrepancy between the experimental and simulated locations of maximum velocities. Despite this, however, the jet centre of mass was calculated and matched well the experimental jet trajectory. Furthermore, while the velocity decays matched well for air, a significant departure between experiment and simulation was observed for helium. It is currently unclear why this departure exists. In general, however, the simulations offered some detailed insight into the overall flow patterns observed in the experiments. Also, the simulations offered some insight into the behaviour of hydrogen.

It was found that flow within a pipe, perpendicular to an upward facing hole, causes the resulting jet to form at an angle relative to the vertical axis, in the direction of the pipe itself. Furthermore, flow separation inside the pipe, at the orifice, and curvature of the pipe, relative to the size of the hole, are believed to generate the asymmetric flow patterns observed. As a result, the location of maximum velocity is misaligned with the centre of mass. Also, in the far field, air and helium were found to have much more jet spreading occurs along the direction of the pipe, compared to all other directions. Hydrogen, however, was found to exhibit axisymmetry, in terms of jet spreading, in the far field. Thus, caution is required when using round jet assumptions to describe the correct dispersion and velocity decay of the gas in realistic geometries.

The authors would like to acknowledge the Natural Sciences and Engineering Research Council of Canada (NSERC) for project funding, and Compute Canada for computational resources.

1. Chernyavsky, B., Wu, T.C., Péneau, F., Bénard, P., Oshkai, P. and Djilali, N., Numerical and experimental investigation of buoyant gas release: Application to hydrogen jets, *Int. J. Hydrogen Energy*, **36**, (2011), pp. 2645–2655.
2. Panchapakesan, N.R. and Lumley, J.L., Turbulence measurements in axisymmetric jets of air and helium. Part 1. Air jet, *J. Fluid Mech.*, **246**, (1993), pp. 197–223.

3. Hussein, H.J., Capp, S.P. and George, W.K., Velocity measurements in a high-Reynolds-number, momentum-conserving, axisymmetric, turbulent jet, *J. Fluid Mech.*, **258**, (1994), pp. 31–75.
4. Amielh, M., Djeridane, T., Anselmet, F. and Fulachier, L., Velocity near-field of variable density turbulent jets, *Int. J. Heat Mass Transfer*, **39** (10), (1996), pp. 2149–2164.
5. De Gregorio, F., Free compressible jet investigation, *Exp. Fluids*, **55**: 1693 DOI 10.1007/s00348-014-1693-9.
6. Quinn, W.R., On mixing in an elliptic turbulent free jet, *Phys. Fluids A*, **1** (1), (1989), pp. 1716–1722.
7. Mi, J. and Nathan, J., Statistical Properties of Turbulent Free Jets Issuing from Nine Differently-Shaped Nozzles, *Flow Turbul. Combust.*, **84**, (2010), pp. 583–606.
8. Su, L.K., Helmer, D.B. and Brownell, C.J., Quantitative planar imaging of turbulent buoyant jet mixing, *J. Fluid Mech.*, **643**, (2010), pp. 59–95.
9. Soleimani nia, M., Maxwell, B.M., Oshkai, P. and Djilali, N., Concentration in Turbulent Multi-Component Jets: A Quantitative Imaging Approach, 7th International Conference on Hydrogen Safety, Hamburg, Germany.
10. Chakravarthy, V.K. and Menon, S., Linear eddy simulations of Reynolds number and Schmidt number effects on turbulent scalar mixing, *Phys. Fluids*, **13**, (2001), pp. 488–499.
11. Vanella, M., Piomelli, U. and Balaras, E., Effect of grid discontinuities on large-eddy simulation statistics and flow fields, *J. Turbul.*, **9**: 32, (2008), pp. 1–23.
12. Shyue, K.M., An efficient shock-capturing algorithm for compressible multicomponent problems, *J. Comput. Phys.*, **142**, (1998), pp. 208–242.
13. Hou, T.Y. and LeFloch, P.G., Why nonconservative schemes converge to wrong solutions: Error analysis, *Math. Comput.*, **62**, (1994), pp. 497–530.
14. Gottlieb, J.J. and Groth, C.P.T., Assessment of Riemann solvers for unsteady one-dimensional inviscid flows of perfect gases, *J. Comput. Phys.*, **78**, (1988), pp. 437–458.
15. van Leer, B., Towards the ultimate conservative difference scheme III. Upstream-centered finite-difference schemes for ideal compressible flow, *J. Comput. Phys.*, **23**, (1977), pp. 263–275.
16. Falle, S.A.E.G. and Giddings, J.R., Numerical Methods for Fluid Dynamics IV, Oxford University Press, chapter Body capturing using adaptive cartesian grids, 1993, pp. 337–343.
17. Mitran, S.M., Adaptive Mesh Refinement Computation of Turbulent Flows - Pitfalls and Escapes, Numerical Modeling of Space Plasma Flows: ASTRONUM 2008 (N.V. Pogorelov, E. Audit, P. Colella and G.P. Zank, eds.), ASP Conf. Series, volume 406, 2009, pp. 249–254.
18. Klein, M., Sadiki, A. and Janicka, J., A digital filter based generation of inflow data for spatially developing direct numerical or large eddy simulations, *J. Comput. Phys.*, **186**, (2003), pp. 652–665.
19. Eggels, J.M., Unger, F., Weiss, M.H., Westerweel, J., Adrian, R.J., Friedrich, R. and Nieuwstadt, F.T.M., Fully developed turbulent pipe flow: a comparison between direct numerical simulation and experiment, *J. Fluid Mech.*, **268**, (1994), pp. 175–209.
20. Witze, P.O., Centreline velocity decay of compressible free jets, *AIAA Journal*, **12** (4), (1974), pp. 417–418.
21. Vogel, J.C. and Eaton, J.K., Combined heat transfer and fluid dynamic measurements downstream of a backward-facing step, *J. Heat Transfer*, **107** (4), (1985), pp. 922–929.
22. Gharib, M. and Roshko, A., The effect of flow oscillations on cavity drag, *J. Fluid Mech.*, **177**, (1987), pp. 501–530.
23. Zaman, K.B.M.Q., Asymptotic spreading rate of initially compressible jets-experiment and analysis, *Phys. Fluids*, **10** (10), (1998), pp. 2652–2660.